J. Fluid Mech. (1995), *vol.* 287, *pp.* 383–403

Cavitation in the rotational structures of a turbulent wake

By B. BELAHADJI, J. P. FRANC AND J. M. MICHEL

Laboratoire des Écoulements Géophysiques et Industriels – Institut de Mécanique de Grenoble, Institut National Polytechnique de Grenoble et Université Joseph Fourier, BP 53, 38041 Grenoble Cedex 9, France

(Received 26 January 1994 and in revised form 1 November 1994)

Experiments show that cavitation, if moderately developed, makes three kinds of vortical coherent structures visible inside the turbulent wake of a two-dimensional obstacle: Bénard–Kármán vortices, streamwise three-dimensional vortices and finally the vortices which appear on the borders of the very near wake. The latter, which are called here *near-wake vortices*, result by successive pairing in the first ones and there is some indication that they are also the origin of streamwise vortices. Cavitation is not a passive agent of visualization, as can be established on the basis of fundamental arguments, and it reacts with the flow as soon as it appears; when it is developed, it breaks the connection between the elongation rate and the vorticity rate of the vortex filaments. Then the subsequent evolution of a cavitating vortex and its final implosion are rather complicated. Despite its active character, cavitation in rotational structures, if properly interpreted, can give information of interest on the basic non-cavitating turbulent flow. By adapting a simple model due to Kermeen & Parkin (1957) and Arndt (1976), and counting near-wake vortices, it is possible to accurately predict the conditions of cavitation inception: consideration of coherent rotational structures is probably the best approach to explain, in an almost deterministic way, the large difference between the absolute value of the mean pressure coefficient at the obstacle base and the incipient cavitation number.

1. Introduction

For a long time, the inception of cavitation in turbulent shear flows was an important topic of experimental research, as is shown in the standard textbook by Knapp, Daily & Hammitt (1970). Safety problems in hydraulic or nuclear power plants stimulated the interest in these studies: it was known that cavitation could appear around submerged, rapid liquid jets evolving in a high ambient pressure field. The risk of cavitation was then generally estimated by considering pressure fluctuations as related to the local turbulence of the flow. Of course, such a statistical approach gave at most r.m.s.-values of pressure fluctuations, so that the crest values of the temporal underpressures remained unknown. A notable exception must be mentioned: the experimental works of Kermeen & Parkin (1957) on flows around circular disks, in which the dependence of the incipient cavitation number on the Reynolds number was demonstrated, isolated vortices in the shear layer were visualized and a simple model was proposed, later taken up again and developed by Arndt (1976); however, those authors failed to obtain the value of the two main parameters of that model, i.e. the size and the rotation rate of the vortices.

More recently, the interest in cavitating turbulent flows reappeared as a consequence

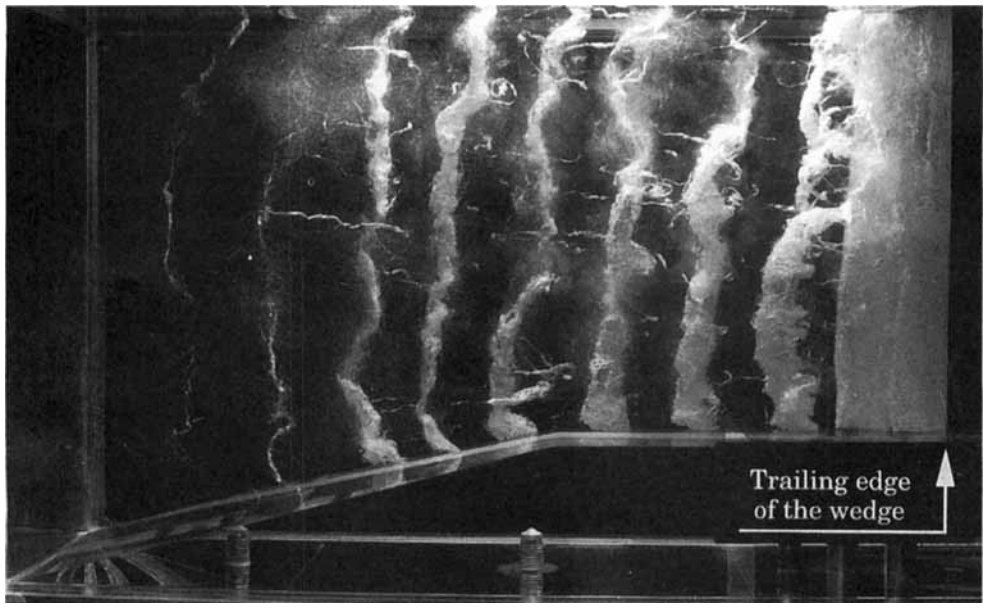

FIGURE 1. Flow behind the vertical wedge – effect of the elongation rate of the Bénard–Kármán vortices: $Re = 3.6 \times 10^5$; $\sigma_c = 1.57$; $S = 0.311$ (flow from right to left; the dimensions are given in figure 3).

of two main factors. Firstly, the acceptance of developed cavitation has become current in engineering practice, once erosion dangers have been ruled out, while several experimentalists have observed that erosion damage in rotating machinery occurs more easily if distinct cavitating vortices, initially released from attached cavities, collapse in regions of adverse pressure gradient (see for instance Soyama, Kato & Oba 1992). Secondly, research in turbulence has been renewed by the consideration of discrete, coherent rotational structures (see e.g. the textbook by Lesieur 1992) and it is hoped that cavitation studies can take advantage of that new look, having it contributed to the evidence for the three-dimensional streamwise vortices (Franc, Michel & Lesieur 1982).

In the present paper, we study the global conditions of inception and development of cavitation inside the discrete rotational structures of a turbulent wake and its subsequent disappearance downstream. That cavitation appears firstly in intense enough vortices ensues from physical experience such as related in Young & Holl (1966) and the previously mentioned paper by Franc *et al.* It also follows experience from numerical treatments which, at least in the case of shear flows, tend to identify the regions of high vorticity with the regions where pressure is low (Douady, Couder & Brachet 1991; Métais & Lesieur 1992). That result also agrees with the pressure equation in which the source term 'vorticity intensity' plays a prominent role in the production of low pressures, due to its high degree of concentration on very thin vortex filaments. Little work has been done on cavitation development in turbulent vortices, and we have to examine it with reference to rather simpler cases, for instance cavitating toroidal vortices (Genoux & Chahine 1983) or cavitating tip vortices (Ligneul 1989). Finally, in view of industrial applications and erosion risks, consideration is also given through the paper to cavitation disappearance, although its main purpose is rather fundamental aspects of fluid mechanics.

Section 2 of the paper is devoted to some basic, though simple, considerations on

cavitating vortices. The experimental methods and set-up, together with an overview of the cavitating wake, are described in §3. The three following sections deal with the different kinds of vortices that cavitation makes visible. In particular, §6 presents a simple physical model, suited to the present configuration, from Arndt's (1976) ideas, which requires the counting of the so-called *near-wake vortices*. That is possible by means of rapid cinematography, for both cases of developed and incipient cavitation, due to several favourable factors of the present flow configuration. The results of the model agree well enough with the experimental results on cavitation inception; then the large discrepancies between the incipient cavitation number and the absolute value of the local pressure coefficient are clearly explained, and it is hoped that the present method will be valuable for the prediction of cavitation occurrence in other shear flow configurations.

2. Basic ideas

A preliminary remark relates to the geometry of the vortex filaments. If they are loci of low pressure with respect to the surrounding flow, all modifications of the cavitating state inside those filaments must be made according to either the radial or the axial mode. In a strictly two-dimensional flow, only the radial mode can be expected. In three-dimensional flows, both modes are possible and are actually observed. For instance, in a region of adverse pressure gradient, the start of cavitation disappearance often manifests itself by the pinching of a cavitating three-dimensional vortex (see for instance the last vortex on the left side of figure 1): there, the flow is mainly two-dimensional and the cavitation evolution can be considered as locally radial.

Now, let us consider a *near-wake vortex*, such as the ones described in §§3 and 6 (see figures 4 and 5), at the instant it is created just downstream the wedge. Experiment shows that cavitation appears in a very short time, of the order of 0.1 ms, on the entire length of the vortex, i.e. the channel height equal to 21 cm. Then the local flow can be considered as practically two-dimensional and we can use mass conservation to estimate the ratio between the diameter D_v of the visible cavitating vortex and the diameter D_l of the initial liquid core which is transformed into vapour. With the corresponding index for the vapour and liquid densities, we have

$$\frac{D_l}{D_v} \approx \left(\frac{\rho_v}{\rho_l}\right)^{1/2};$$

for water at room temperature, the value of the root is about 1/230. The smaller visible filaments have a diameter D_v of 0.5 mm, so that the corresponding liquid core diameter is about 2 μm. That size must be compared to the size of the region in which significant variations of the pressure near the vortex core take place. As a rough estimate, we take the expression $\rho_l \omega^2 r^2/2$, where ω is the rotation rate. With a value of 500 Pa for the pressure variations and, according to the ω-value obtained afterwards, we find 0.1 mm for the radius. Thus, vaporization concerns only a small fraction of the underpressure region defined within a possible uncertainty of 500 Pa. Both orders of magnitude show that measurement of the underpressure crest values is really not possible with the available techniques since the pressure transducer size clearly exceeds the values just found. From the viewpoint of numerical shear flow simulation, the small size of the depression regions also seems to be a useful indicator of their low density of probability.

The conclusion regarding the ratio of diameters would not be changed significantly if one considered that the cavitating near-wake vortices result from the explosion of

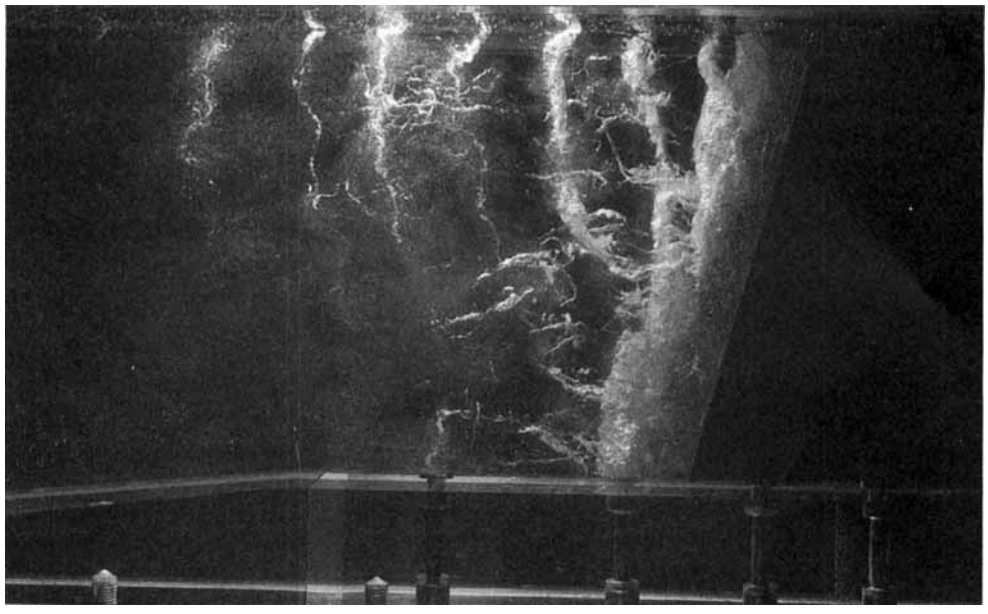

FIGURE 2. Axial collapse of the Bénard–Kármán vortices in the case of an inclined wedge: $Re = 2.6 \times 10^5$; $\sigma_c = 1.75$; $S = 0.331$ (flow from right to left).

some air nuclei entrapped in their core. If that case arose, the conditions of nuclei instability (Ligneul 1989) could be yet less severe and the extent of the underpressure region could possibly be different from the one previously estimated. However, the present experimental conditions lead us to rule out the nuclei effect since the nuclei concentration is usually lower than 0.1 per cm^3 (Briançon-Marjollet, Franc & Michel 1990) when the hydrodynamic tunnel water is not seeded with air nuclei. Such a value suggests that it is most unlikely to have a nucleus present in each near-wake vortex whose size is less than 2 mm in diameter and about 20 cm in length. Thus, we prefer to interpret cavitation inception as due to the continuous vaporization of the vortex core. That is plausible since the basic vortex theorems ensure that vortex lines are material lines when the viscosity effects are neglected: the liquid particles tend to follow the regions of lower pressures, thus increasing the time available for their vaporization.

The last point which deserves examination is the behaviour of the vortices in which cavitation is well developed, like the ones seen on photographs of figures 1, 2 and 4. From the previously mentioned theorems, in incompressible and inviscid fluids the rotation rate ω of a non-cavitating vortex filament is connected to its length δl by the relation $\omega/\delta l = k$, where k is a constant (see for instance Batchelor 1967). That result does not hold for the cavitating vortex whose vapour core radius can evolve independently from its length as a result of variations of the external pressure field. In fact, with a constant circulation around the vortex filament, the rotation rate varies inversely with the axial moment of inertia. In other words, cavitation tends to break the link between the elongation rate and the rotation rate of a rotational filament.

Two main consequences are expected. Firstly, the evolution of a cavitating vortex can be thought as dependent on both the external pressure field – due either to the global flow configuration or to the neighbouring vortices – and the self-induced underpressure due to its own vorticity. When the vortex travels through the flow region, it undergoes elongation and changes in the ambient pressure at once. If the

ambient pressure is constant, the main effect of elongation is an increase of the rotation rate which tends to develop cavitation. That can be seen in the photograph of figure 1 in which cavitation appears more developed in the lower part of the Bénard–Kármán vortices. In that region the cavitating vortices benefit from the boundary layer elongation rate as is shown by their direction, roughly at 45° to the wall. The effect of the ambient pressure variations is twofold when the length of the vortex filament is kept constant: on the one hand, an increase of that term results in a reduction of the vaporous rotational cavity radius; on the other hand, the volume reduction is accompanied by an increase of the rotation rate. That secondary, antagonistic, effect can give rise to natural oscillations in the case of isolated vortices, either two-dimensional (Franc 1982) or toroidal (Genoux & Chahine 1983). In the present experiments, natural oscillations, as far as they can be defined for the intricate vortices networks we have to consider, have not been observed.

The second consequence concerns the motion, relative to the liquid medium, of rotational cavities which otherwise undergo volume variations. It is natural to think – although not easy to model – that volume variations affect the translational cavity velocity by a kind of variable virtual mass. Such an effect is probably observed for the primary two-dimensional Bénard–Kármán vortices, as it will be shown in §4 of the paper.

At this point, it becomes obvious that cavitation does not constitute a passive agent for the visualization of the turbulent wake flow. When it is largely developed, it ultimately destroys the near-wake structure since it replaces it by a continuous vapour supercavity. But even at its inception it modifies the basic flow as vaporous cavities need a very large volume in comparison with the liquid in which they originate. For the moderate development of cavitation we consider here, it is however believed that the original wake topology is kept. Thus, aside from its interest for cavitation, such a study is able to add useful information about the basic non-cavitating flow.

3. Experimental methods

3.1. *The water facility*

The flow is produced in the first (a closed one) of the two test channels of the Hydrodynamic Tunnel of LEGI-IMG (Briançon-Marjollet & Michel 1990). The symmetrical wedge (base $b = 35$ mm, triangle side $l = 80$ mm and obstruction ratio = 0.2) is held either vertically or inclined in a part of the test section which has a restricted area and a rectangular section of 175 mm in width and 210 mm in height (see figure 3). In this region, the water velocity, V_c, is adjustable between 4 and 15 m s^{-1} so that the Reynolds number, $Re = V_c b/\nu$, varies from 1.2×10^5 to 5.2×10^5. By means of a vacuum pump, the pressure p_c in the restricted area can be regulated so that the cavitation parameter, $\sigma_c = 2(p_c - p_v)/\rho V_c^2$ (where p_v is the vapour pressure) can take values from 0.1 to about 7. All our measurements are carried out in the domain corresponding to values greater than 1, in which the shedding of vortices occurs in a discrete and coherent way. This corresponds to the case of cavitation inception or developed cavitation but not an attached cavity.

The test section allows us not only to study the dynamics and kinematics of the vortices but also their erosive potential due to their axial collapse. Indeed, two geometrical elements might favour this implosion: (i) the divergent part of the test section, where an important dissymmetrical pressure field occurs and (ii) the use of inclined wedges. The latter allows cavitating vortices which enter this pressure field to be subject to different pressures at their two extremities. The photograph of figure 2

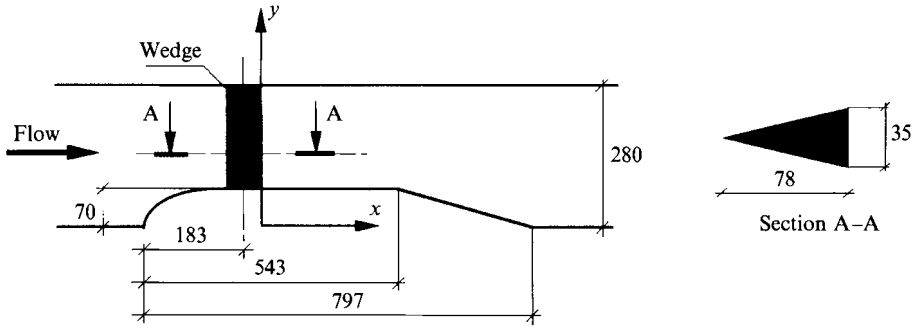

FIGURE 3. Test section (side view). Dimensions in mm.

shows a case for which the implosion of cavitating vortices actually follows the expected axial mode. But in other cases very different structures of the cavitating wake could be observed in the divergent region, with a later extinction of cavitation either at mid-height of the channel or in the bottom boundary layer. That illustrates the influence of the vortex elongation rate on the evolution of cavitation, in addition to the pressure influence, already mentioned in §2.

A pressure transducer (model PCB H 111 A 21, with diameter 5.55 mm and natural frequency 300 kHz) was mounted flush on the top wall of the channel, at abscissae 220 or 320 mm from the wedge base. It gives a periodic signal with a frequency which is twice the shedding frequency f of the primary vortices in non-cavitating conditions and with an amplitude of about 3000 Pa when the velocity is around 10 m s^{-1}. The amplitude increases up to 15000 Pa when cavitation becomes more developed and then it decreases for the lower values of the cavitation number, between 1.7 approximately and 1. The important point is that very narrow pressure peaks appear in the cavitating regime, the duration of which being less than 10 μs while their crest value can reach 50 MPa. That value is probably underestimated by the effect of the transducer size, but it indicates the damage potential of such cavitating flows. As those pressure peaks generally appear at instants when the basic periodic signal is at its maximum, they are associated with the collapse of bubbles turning around the main vortices rather than to collapse of cavitating vortices themselves.

3.2. *An overview of the wake structure*

In the present experiments, the structure of the wake is revealed by visualization of the reflecting interfaces between liquid and vapour. Its periodic aspect can be observed with the naked eye using stroboscopic light. Images of the flow are obtained from normal or high-speed photography (6000 and 10000 frames per second, using two different cameras) or from a video. The configuration is such that top views and side views of the channel give complementary information on both two- and three-dimensional aspects of the flow. It must be noted that other measuring techniques, such as hot-film anemometry or laser anemometry, which could theoretically give more detailed information than flow visualization, cannot be used for the study of the present flow.

Three kinds of cavitating rotational structure are visible in the wake of the wedge: the primary, two-dimensional Bénard–Kármán vortices; the secondary, three-dimensional streamwise vortices and the near-wake vortices. All these structures are clearly illustrated in figure 4 and some results related to the appearance and development of cavitation in their core are given in §§4, 5 and 6.

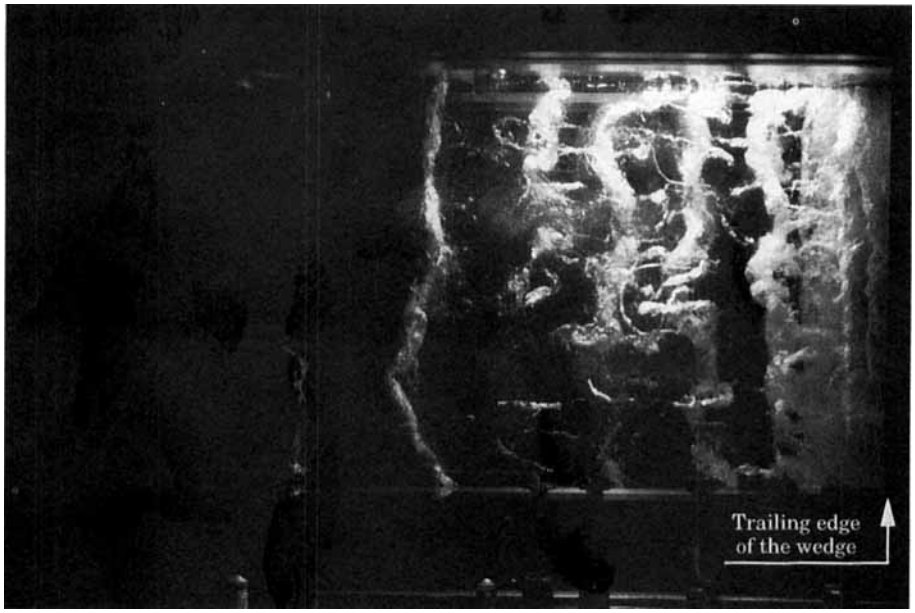

FIGURE 4. Visualization of three kinds of rotational structures in the case of developed cavitation: $Re = 2.5 \times 10^5$; $\sigma_c = 1.75$; $S = 0.293$ (flow from right to left).

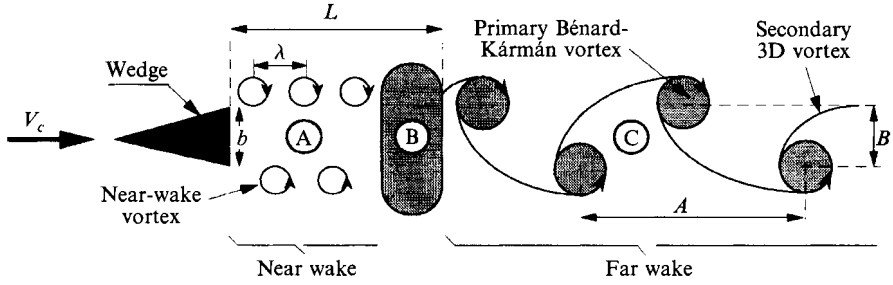

FIGURE 5. Sketch of the wake (top view).

The sketch of figure 5 outlines the three kinds of vortices and shows three regions behind the wedge: A is the near wake, a dead fluid zone, whose length normalized by the wedge base b is roughly equal to 0.7. The near-wake vortices evolve on its borders and are advected up to the region B which in most cases appears as a kind of two-phase mixture. C is the far wake in which the primary and secondary vortices are advected. The normalized length L/b, where L is the distance between the downstream extremity of region B and the trailing edge of the wedge, is about 0.9 when the cavitation is moderately developed and can exceed 4.4 for the lower values of the cavitation parameter. Such results are also found by Ramamurthy & Balachandar (1990) in the study of the near wake of cavitating bluff sources.

An abundant literature has been devoted in the past either to primary two-dimensional vortices in wake flows at moderate and high Reynolds number (see for instance Roshko 1954 and Berger & Wille 1972), or more recently to three-dimensional, streamwise vortices (e.g. Bernal & Roshko 1986 for plane mixing layers; Liepman & Gharib 1992 for the entrainment region of round jets and Meiburg & Lasheras 1988 for plane wakes). Thus, we only have to focus our attention on the

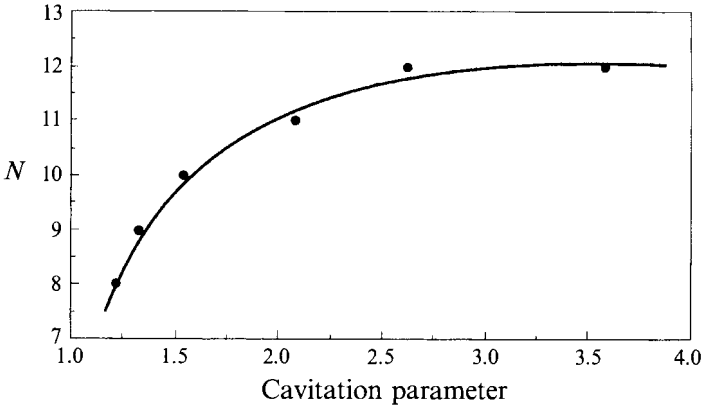

FIGURE 6. Ratio $N = F/f$ versus cavitation parameter.

specific characteristics brought by cavitation to those structures. On the other hand, near-wake vortices, which are not systematically observed in all wakes, are rarely treated and thus deserve more consideration.

The analysis of various high-speed sequences shows that the near-wake vortices, coming out from the two boundary layers, collect in region B and result by successive pairing in the alternate primary Bénard–Kármán vortices. They are produced in a practically periodic way at a frequency F which can be measured by means of films as soon as cavitation appears. That probably results from several favourable circumstances: on the one hand, the solid wall channels tend to impose a negative pressure gradient and then a high vorticity rate on the wedge boundary layers, the thickness of which is very small; on the other hand, the abrupt shape of the body at its base makes the near wake similar to two independent shear layers. Then, the boundary layer vorticity is concentrated in discrete vortices at a rate fixed by the maximum shear layer instability, as will be shown below. As a result, and as much as we can have confidence in flow visualization, the flow produces only two characteristic time scales, namely the shedding periods of near-wake and primary vortices. According to the development of cavitation, frequency F can be from seven to twelve times the frequency f of the primary vortices. Figure 6 illustrates the ratio N between the two frequencies. Its value agrees with that obtained by Kourta *et al.* (1987) for the non-cavitating wake of a circular cylinder at moderate Reynolds number. In that case, vortices of various sizes appear in the near wake, thus creating intermediate time scales. Despite of that difference, for $2000 \leqslant Re < 16000$, the ratio N of the smaller characteristic times to the main primary period is found by those authors to be in the range 4 to 12.

The visualizations of the present study lead us to advance some qualitative propositions in order to describe two global aspects of the cavitating wake. Firstly, as expected, the films clearly show that the vorticity of the Bénard–Kármán vortices comes from the near-wake vortices. The decrease of the number N when cavitation becomes more developed can be understood then if we assume that the maximum area available for the primary vortex in the process of formation inside zone B is imposed by the geometry of the body, i.e. roughly by the square of the wedge base b: when the cavitation parameter decreases, the cross-section area of the cavitating near-wake vortices increases and thus they fill the maximum available area more quickly. That is also corroborated by the increase of the frequency f at the beginning of cavitation development, as it will be shown in the following section. Secondly, a careful

examination of high-speed sequences shows that the primary vortices are ejected violently from zone B when the maximum area is reached, with a velocity which can exceed three times the external velocity, during a very small time in comparison with the main period. Then, the neighbourhood of region B is deeply disturbed until the new vortex already in the process of formation on the other side of the near wake spreads through region B. That transition phase is favourable to the direct ejection of a near-wake vortex from region A to region C without capture by a primary vortex. If that view is correct, such a near-wake vortex can subsequently give birth to a streamwise vortex. That point will be considered again in §5.

4. The primary vortices

4.1. *Strouhal number*

Measurements of the shedding frequencies were conducted using a stroboscope, rapid movies and the pressure transducer. The results of the measurements made with the strobe light are shown in figure 7(*a*) for two Reynolds numbers. The uncertainty in the Strouhal number S defined by $S = fb/V_c$ does not exceed 2.4%.

The Strouhal number depends strongly on the development of cavitation. Indeed, when cavitation develops, the value of S can exceed its value in the non-cavitating regime by 30%. Thus, cavitation has an important effect upon the dynamics of Bénard–Kármán vortices. Furthermore, the shedding frequency f of these vortices increases proportionally with the velocity. This leads to a value of Strouhal number practically independent of the Reynolds number.

The increase of the Strouhal number when the cavitation number decreases down to about 1.7 is consistent with the decrease of the ratio N of frequencies shown in figure 6. But the reason for its subsequent decrease for the lower values of the cavitation number is not clear. Nevertheless, the existence of the maximum is well established and was reported by Young & Holl (1966), Franc (1982) and Ramamurthy & Balachandar (1990). For the high values of σ_c the Strouhal number tends towards a constant value S_{nc} (non-cavitating value) of about 0.25 which will be used hereafter in the model for cavitation inception.

The Strouhal number S normalized by its non-cavitating value S_{nc} is represented on figure 7(*b*) as a function of the normalized cavitation number σ/σ_i, where σ_i is the incipient cavitation parameter (see §6.2). It can be seen that, for the same Reynolds number of 2.0×10^5 and approximately the same wedge apex angle, the present data agree with the measurements made by Young & Holl (1966).

4.2. *Vortex streets*

Measurements of the wavelength A and the distance B between the vortex streets are made from the top-view photographs, especially of the first vortices released from region B. The ratio of the distance B to the wavelength A is about 0.07 for the lower values of σ_c and tends towards an asymptotic value of the order 0.28 when σ_c increases (see figure 8). This value is the same as that which ensures the stability of a Kármán vortex street in the case of a non-cavitating regime (Milne-Thomson 1968). In other words, when cavitation is sufficiently developed, the spacing B between the vortex streets decreases by about 80% in comparison with that of the subcavitating flows. This mechanism of narrowing of the vortex street, which was not elucidated until now, shows the strong interaction between cavitation and the basic flow and thus the important effect of cavitation on the physical properties of the Kármán vortex street. The bars on figure 8 represent the uncertainty in the ratio B/A.

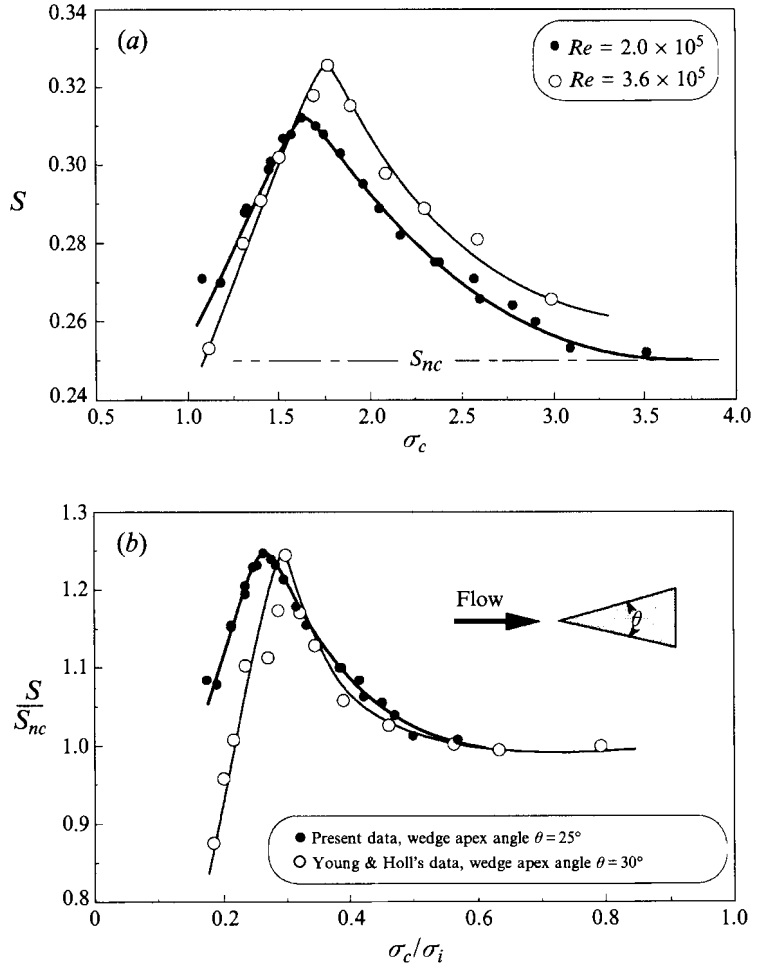

FIGURE 7. Strouhal number of the primary vortices: (*a*) Strouhal number versus cavitation parameter; (*b*) comparison with Young & Holl's data ($Re = 2.0 \times 10^5$).

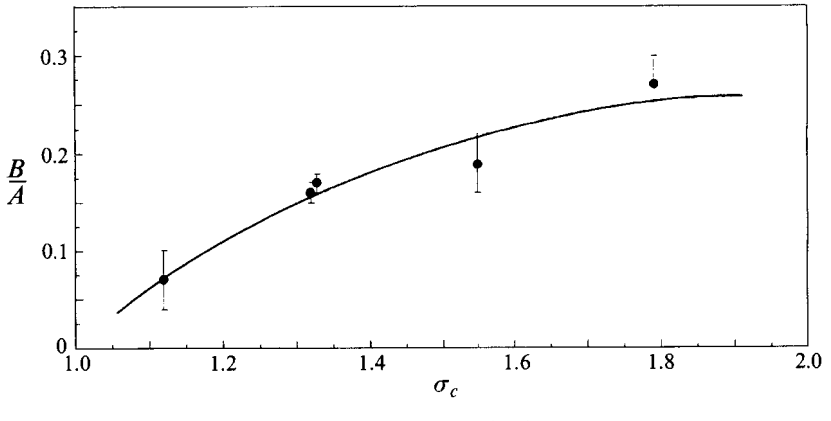

FIGURE 8. Ratio B/A versus cavitation parameter.

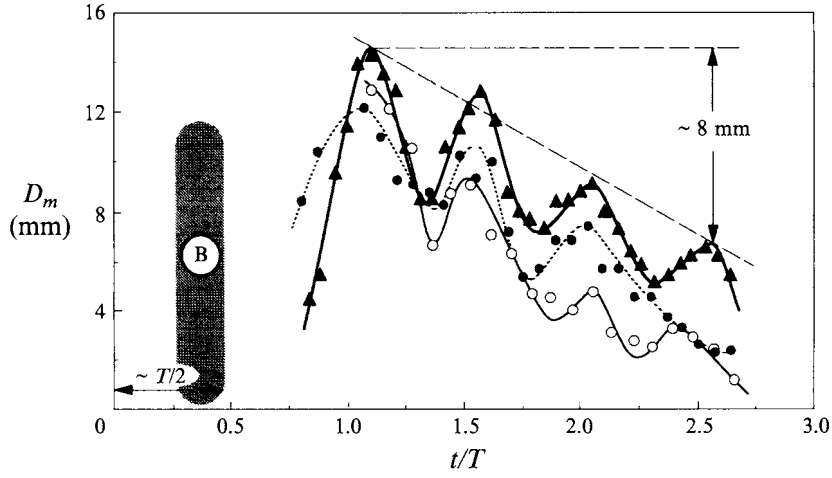

FIGURE 9. Temporal variation of the mean diameter ($T = 1/f$); ●, $Re = 3.6 \times 10^5$, $\sigma_c = 1.47$, $S = 0.297$, $f = 90.5$ Hz (movie 9); ○, $Re = 4.2 \times 10^5$, $\sigma_c = 1.84$, $S = 0.293$, $f = 101$ Hz (movie 13); ▲, $Re = 3.1 \times 10^5$, $\sigma_c = 1.33$, $S = 0.293$, $f = 72$ Hz (movie N10).

4.3. *Temporal evolution*

The high-speed sequences of about 7500 frames per second (twenty-six films in total) allow measurements of the positions and motions of vortices in the wake. Using a projector system for the films, the temporal evolution of vortices is shown with a good precision since this system allows the following of the frame-by-frame movement of each vortex which evolves over more than 400 frames. By this means, flow details are obtained and the most interesting results are presented here.

The acquisition of geometrical data (diameter, length, position) over time gives results concerning the elongation rate and velocity of the vortices. Because of the non-uniformity of the diameter of the vortex, we consider the mean diameter D_m which is, for a given position, the average of twenty measurements along the channel height. The fluctuations of the mean diameter, due to the pressure fluctuations, are illustrated in figure 9. Their amplitude tends to decrease far from the wedge. Their frequency is twice the shedding frequency of the primary vortices, while the maximum values of the diameter coincide in time with the release of those vortices from region B. Thus, the shedding of the primary Bénard–Kármán vortices imposes pressure fluctuations over the downstream region of the wake, the extent of which is at least three wavelengths. In the meantime, the length of the cavitating primary vortices does not undergo any observable periodic fluctuations. That illustrates the fact already mentioned that cavitation breaks the connection between the elongation rate and the vorticity rate of the rotational filaments. Note that in figures 9 and 10 the time origin is chosen so that the whole life of the vortex, including its formation in region B, is taken into account.

Figure 10 shows an example of the temporal evolution of the vortex axis velocity. We clearly observe the re-entrainment of the vortex by the external flow. The velocity of the vortex, initially affected by the wake deficit profile, tends towards a value which is that of the mean flow in the absence of the obstacle. The mean ratio between the two velocities is about 76% ($\pm 10\%$).

Similarly to the diameter, the instantaneous advection velocity of the primary vortices is affected by the pressure fluctuations but in an opposite phase: the high velocities of the vortices coincide with their thinning phase. The advection velocity fluctuations are not negligible since their amplitude can reach values of the order 1 to

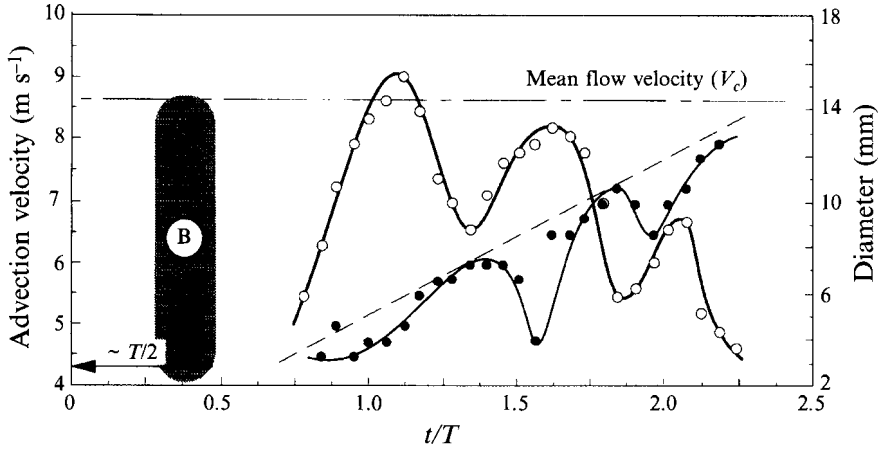

FIGURE 10. Temporal variation of diameter (—○—) and advection velocity of vortex axis (—●—), $Re = 3.128 \times 10^5$; $\sigma_c = 1.33$; $S = 0.293$; $f = 72$ Hz; $V_c = 8.61$ m s^{-1}.

2 m s^{-1}. This fact was systematically observed in all the high-speed sequences. It seems to express the effect of the added mass of rotational cavities (see § 2). However, it is also possible that it combines with a kind of flow blockage due to the increase or decrease of all cavitating vortex volumes according to the pressure variations imposed by the release of the primary vortices.

In one case only ($Re = 3.12 \times 10^5$, $\sigma_c = 1.33$), was it possible to estimate the rotation rate of the primary cavitating vortices from a high-speed sequence. It was about ten times less than the rotation rate of the near-wake vortices. Three mechanisms can explain that low value. Firstly, for the small σ_c value considered, cavitation is largely developed, the vortex diameters are large and therefore this tends to increase their rotational inertia. Secondly, a part of external potential flow can be captured by the primary vortices together with the near-wake vortices, thus diminishing the total vorticity rate. Finally, each primary vortex is in contact with the preceding and the following ones of the other street and exchanges of opposite circulations between both streets are then possible (Berger & Wille 1972).

5. The secondary vortices

As pointed out in § 3, superimposed on the primary spanwise vortices are secondary streamwise vortices. The interaction between the two structures is clearly observed on the photographs of figures 11 and 12. For many years, particular attention has been devoted to the study of the secondary vortices. The computational studies by Corcos & Lin (1984) and Lin & Corcos (1984) and the experimental ones by Lasheras, Cho & Maxworthy (1986) and Meiburg & Lasheras (1988), show that the origin of three-dimensional vortices lies in the instability of the strain regions (braids) formed as the primary, two-dimensional, Kelvin–Helmholtz instability develops. The interaction of the streamwise structures with the spanwise Kármán vortices induces strong undulations in the core of the latter.

For the high Reynolds numbers we consider here, the wake is strongly turbulent. Thus, it is possible to assign with some reliability neither the true origin of the three-dimensional instabilities, nor a schematic representation of the development of those instabilities like that proposed by Lasheras & Cho (1988). However, there is a close similarity between the final stage of the development suggested by those authors and

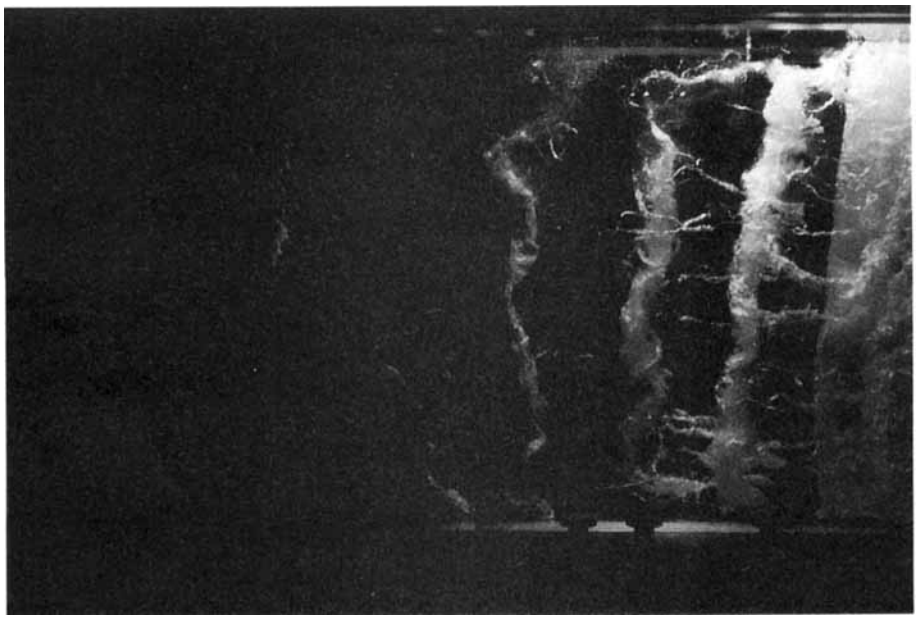

FIGURE 11. Interaction between the primary and the secondary vortices: $Re = 4.3 \times 10^5$; $\sigma_c = 1.32$; $S = 0.286$ (side view photograph, flow from right to left).

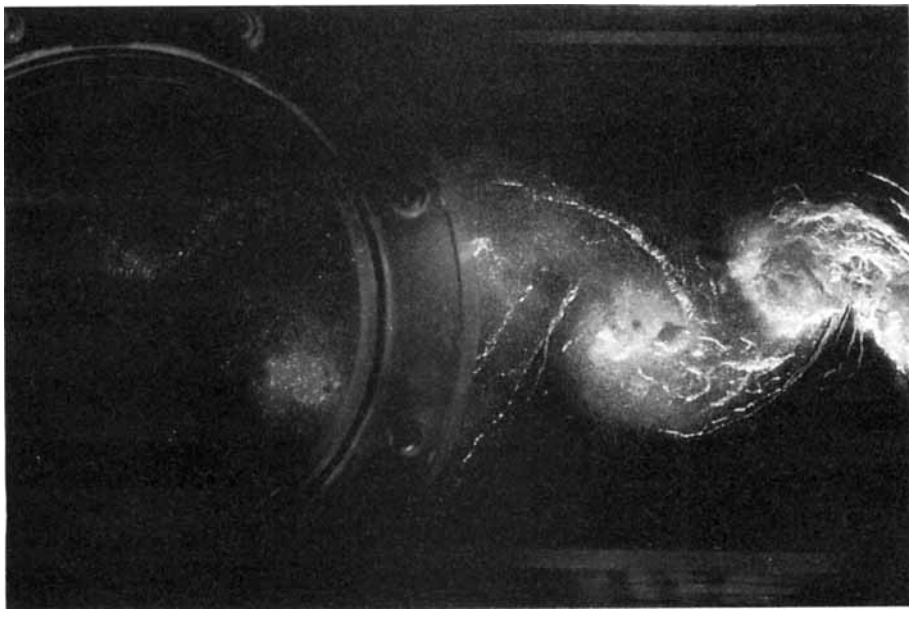

FIGURE 12. Top view of the primary and the secondary vortices: $Re = 2.7 \times 10^5$; $\sigma_c = 1.79$; $S = 0.301$ (flow from right to left).

the manner in which the primary and secondary vortices interact in our experiments. This resemblance is all the more prominent since the same anchorage structures are observed in both cases. Furthermore, as previously discussed, it seems that the secondary vortices come from the near-wake vortices which are not collected into

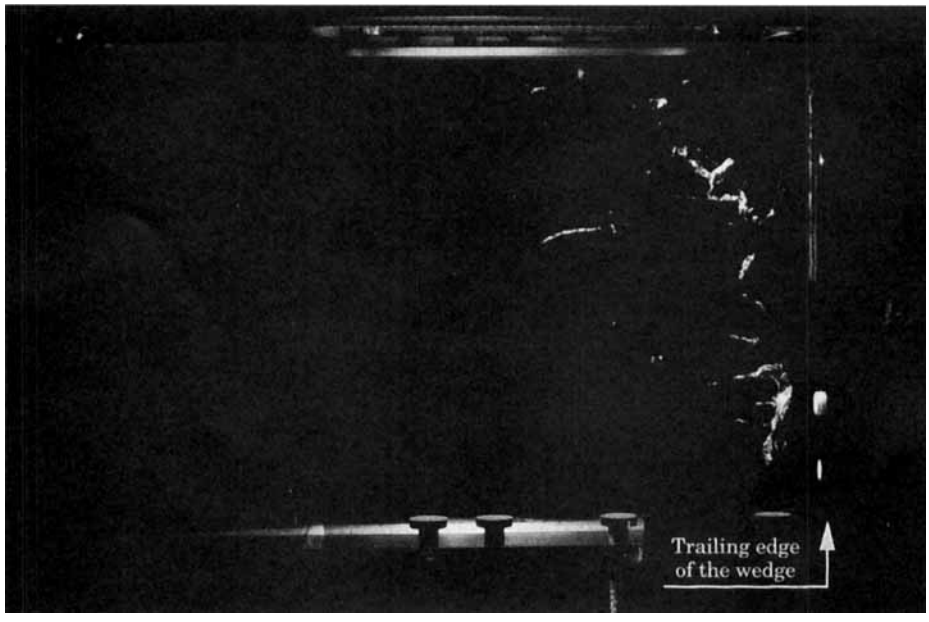

FIGURE 13. Visualization of small cavitating filaments in the case of conditions close to cavitation inception: $Re = 3.0 \times 10^5$; $\sigma_c = 3.72$ (flow from right to left).

	X_m (mm)	n	D_m (mm)	L_m (mm)	ξ
$Re = 3.6 \times 10^5$; $\sigma_c = 1.87$	95	7	2.4	47.0	0.68
	120	8	2.0	52.7	0.61
	140	8	1.8	56.4	0.62
	160	7	1.8	51.7	0.63
	200	6	1.6	55.2	0.67
$Re = 4.2 \times 10^5$; $\sigma_c = 1.84$	90	7	3.0	46.6	0.66
$Re = 3.6 \times 10^5$; $\sigma_c = 1.47$	108	7	3.5	49.5	0.62

TABLE 1. Secondary vortices' characteristics

region B and then are strongly stretched between two adjacent primary vortices. This conclusion must be considered with some caution, however, as it is not founded on direct observation, but is rather suggested by consideration of the events which may occur when the ejection of a primary vortex disturbs the wake.

In order to study the streamwise vortices and their interaction with the spanwise structures, many photographs as well as cinematography and video recordings were used. A statistical analysis of those images has been undertaken. It consists, for various flow configurations, in counting the number n of the secondary cavitating vortices, in measuring their mean length L_m, diameter D_m and the normalized distance ξ ($\xi = 2s/A$, where s is the mean distance between adjacent secondary structures). The latter are made in the restricted area of the test section and especially near region B where most of the streamwise vortices are made visible by cavitation and therefore taken into account in our statistics. Indeed, because of their high vorticity, those structures are among the first ones in which cavitation occurs (see figure 13). Katz & O'Hern (1986) found the same phenomenon for mixing layers in water.

Table 1 illustrates the main results concerning the secondary vortices. X_m is the mean

distance between the wedge trailing edge and the middle of the two adjacent primary vortices where the streamwise vortices are considered. It is shown that, independently from the Reynolds number, there are about seven *cavitating secondary vortices* stretched between two adjacent primary vortices and disposed over the height of the flow, i.e. 210 mm. This corresponds to a mean normalized distance ξ of about 0.64, practically independent of the level of cavitation development. The same value is obtained by Bernal & Roshko (1986) in the case of a mixing layer. It is also shown that the mean diameter increases from about 1.5 to 3.5 mm when cavitation becomes more developed. A complementary study (Filali 1993) has shown that the development of cavitation results in the increase of the number of long cavitating vortices while the number of small ones decreases: then, it can be inferred that the development of cavitation is made over a limited fund of available streamwise vortical structures.

6. The near-wake vortices

The near-wake vortices are periodically produced by the two boundary layers which develop on the sides of the wedge (see figure 5). Although their vorticity comes from those boundary layers, they are probably separated in coherent structures by the strong instability of the shear layers which limit the dead fluid zone A: that will be shown more clearly hereafter. Their rotation rate is high so that cavitation occurs in their core well before the primary Bénard–Kármán vortices.

6.1. *Main experimental results*

All the results presented hereafter are obtained by analysis of high-speed movies. The local reference parameters are: the pressure, p_s, or the pressure coefficient, $C_{p_s} = 2(p_s - p_c)/\rho V_c^2$, measured at the wedge base by a simple tube and a relative mercury manometer; the velocity of the external flow, $V_s = V_c(1 - C_{p_s})^{1/2}$.

The cavitating near-wake vortices are visible at about 5 mm from the trailing edge of the wedge. They are first advected with a velocity equal to $V_s/3$. During their displacement toward region B, they are accelerated by the external flow up to higher velocity values of the order $3V_s/4$. Some of them pair before entering zone B. In that case, the diameter of their vapour core increases from 1 to about 4 mm (more detailed information can be found in Belahadji 1993).

In connection with their acceleration, the wavelength λ of the near-wake vortices, i.e. the distance between two consecutive vortices (see figure 5), increases when they are advected downstream. A typical spatial evolution of λ is represented on figure 14 versus the mean abscissa X_m. For given Reynolds number and cavitation parameter, λ increases with X_m.

The wavelength λ_s, just at the exit of the wedge, is about 4 mm (see figure 14). Like in the theory of stability of free shear layers, it is appropriate to normalize this parameter by $\alpha = \pi h/\lambda_s$, where h is the boundary layer thickness estimated from the plane plate formula (Schlichting 1987). For the previous conditions, i.e. $Re = 3.15 \times 10^5$ and $\sigma_c = 1.33$, α is equal to 0.38. Note that the near-wake vortices are generated by the Kelvin–Helmholtz instabilities of the shear zones of the wake. Such zones, as mentioned in Drazin & Reid (1981), are unstable for perturbations such that the normalized wavelength α is in the range 0–0.64. Moreover, the maximal perturbation occurs when $\alpha = 0.4$. This value is quite comparable with that obtained in our case.

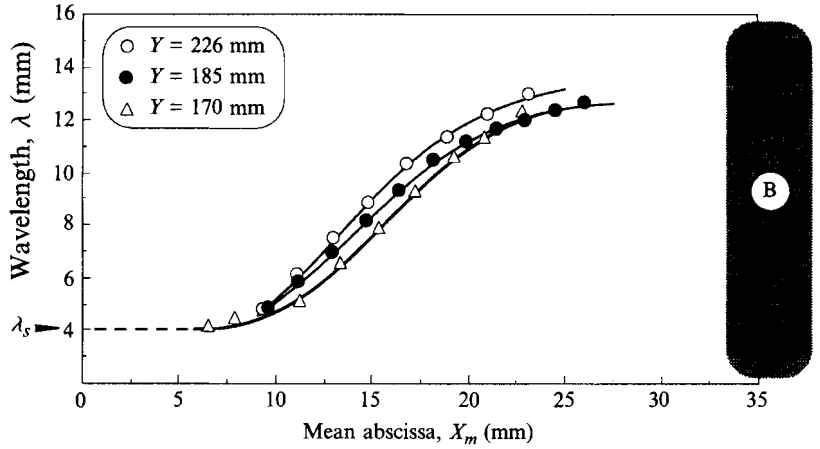

FIGURE 14. Spatial evolution of the wavelength of the near-wake vortices: $Re = 3.15 \times 10^5$, $\sigma_c = 1.33$, $V_s = 12.5$ m s^{-1}, $F = 648$ Hz.

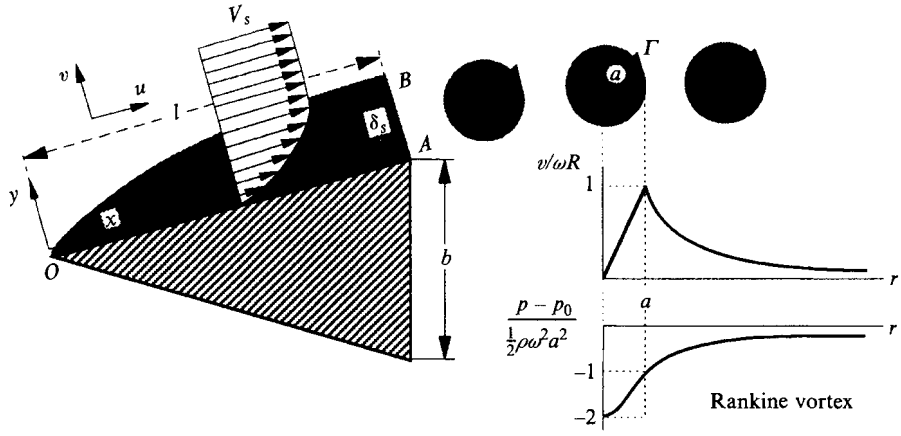

FIGURE 15. Schematic representation of the near wake.

6.2. *A model for cavitation inception*

Observations indicate that cavitation appears in an intermittent way inside the wake in the form of small filaments (see photograph of figure 13). Those filaments belong either to the three-dimensional streamwise vortices or to the two-dimensional near-wake vortices. A criterion of cavitation inception, mainly based on the latter, is deduced from a purely two-dimensional model adapted from the one originally proposed by Arndt (1976) for the flow around a sharp-edged disk.

The near wake of the wedge is idealized by two free shear layers. Each one contains a row of small two-dimensional vortices (see figure 15), considered as Rankine vortices, with a solid rotation core of radius a, circulation $\Gamma = 2\pi a\,\omega a$ and depression $\Delta p = p_{core} - p_s = -\rho[\Gamma/2\pi a]^2$.

Assuming that cavitation occurs when the vortex core pressure, p_{core}, is equal to the vapour pressure, p_v, the critical value of the cavitation parameter can be written in terms of the circulation Γ, radius a and base pressure coefficient C_{p_s}:

$$\sigma_i = -C_{p_s} + 2\left[\frac{\Gamma}{2\pi a V_c}\right]^2. \tag{1}$$

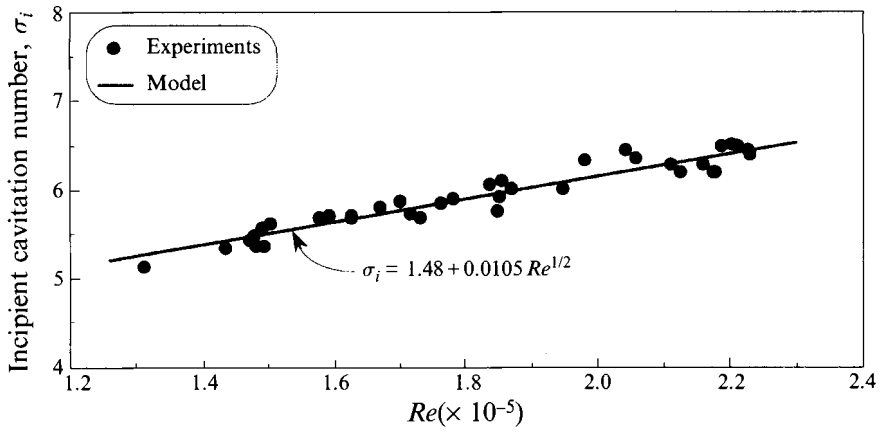

FIGURE 16. Cavitation inception: comparison of model (——) and experiments (●).

Using the measured value of C_{p_s}, the problem reduces to determining the circulation Γ and the radius a. The rotational fluid in the core of each vortex is assumed to be made up of fluid originally in the boundary layer which develops on one side of the wedge. Thus, a and Γ are obtained, when the frequency F is known by examination of high-speed films, from the conservation of mass and vorticity which are shed by the boundary layer at the trailing edges of the wedge sides:

$$V_s(\delta_s - \delta_{1s}) = \pi a^2 F, \quad V_s^2/2 = \Gamma F. \tag{2}$$

In (2), δ_s and δ_{1s} are the boundary layer thickness and the boundary layer displacement thickness respectively. As the obstruction ratio is small, they are approximated by the plane plate formulae (Schlichting 1987):

$$\delta_s = \frac{5l}{(Re_l)^{1/2}} = 5\left(\frac{lb}{Re}\right)^{1/2}, \quad \delta_{1s} = \frac{1.73}{5}\delta_s. \tag{3}$$

Combining equations (1), (2) and (3) (for more details see Belahadji, Franc & Michel 1993), the inception cavitation number can be rewritten in the form

$$\sigma_i = -C_{p_s} + \left(\frac{b}{l}\right)^{1/2} \frac{(1 - C_{p_s})^{3/2}}{26.2\pi} \frac{Re^{1/2}}{NS}. \tag{4}$$

For inception conditions, the ratio N and the Strouhal number S are equal to 12 and 0.25 respectively (see figures 6 and 7*a*). Using the measured value of $C_{p_s} \approx -1.48$, equation (4) is reduced to simply a relationship between the incipient cavitation parameter and Reynolds number:

$$\sigma_i = 1.48 + 0.0105\,Re^{1/2}. \tag{5}$$

As shown in figure 16, the model leads to a forecast of the inception cavitation parameter which is in good agreement with the experimental results. Those are obtained for a limited extent of the Reynolds number: beyond the highest value shown in figure 16, cavitation inception should require higher reference pressures, which cannot be realized in the hydrodynamic tunnel. The high values of the incipient cavitation parameter demonstrate the large influence of the local underpressures, modelled by the second term of equation (5), which by far exceeds the global pressure influence, represented by the first term.

Similar approaches have been made by other authors. They lead to a law $\sigma_i \sim Re^{1/2}$, which correctly predicts the correlation between the incipient cavitation parameter and the Reynolds number although, at higher values of the Reynolds number, deviations from the $Re^{1/2}$ relationship have been observed (Arndt 1976). Among these works, we obviously quote that of Arndt (1976) who empirically adjusted the coefficient of $Re^{1/2}$ in order to make this law explicit. Pauchet, Retailleau & Woillez (1992) used the same model to predict the birth of cavitation in the zone surrounding a cavitating jet. They adjusted the coefficient of $Re^{1/2}$ by using a stability law. In our configuration, the success of the model follows the consideration and the experimental counting of discrete coherent rotational structures: it does not need empirical adjustment and, at the same time, it justifies calling on stability theories when counting is not possible. Of course, the model can be questioned as regards some of its details, for example the choice of the Rankine model for the vortices or the estimate of the boundary layer thicknesses by the plane plate formulae. However, it seems to take into account the essential points of the mechanisms involved in the production of the near-wake vortices.

If we have some confidence in the present approach, we can use relations (2) to estimate the viscous core radius a and its rotation rate ω. For the following conditions: $Re = 1.91 \times 10^5$, $V_s = 7.6$ m s^{-1}, $f = 34$ Hz, we find $a = 1.5$ mm and $\omega = 4800$ rad s^{-1}, which corresponds to about 765 revolutions per second. In other cases, values of ω twice as large can be found while the a value does not undergo large variations. Thus the viscous core diameter is of the same order as the diameter D_v of the vaporous core, already quoted in §2. The ω order of magnitude is approximately given by the transverse gradient of the velocity inside the boundary layer. Comparable or even higher values of the viscous core size and the rotation rate are also given by Arndt, Arakeri & Higuchi (1991) and Fruman *et al.* (1992) in the case of non-cavitating tip vortices. The high value of the rotation rate is synonymous with the deep depression in the core of the vortices, which reaches the order of magnitude of one or several Bar.

7. Further discussion from the viewpoint of turbulence

The near-wake vortices we describe in the present paper exhibit specific characteristics which can be used, in the case of incipient cavitation, as a reference for the numerical computation of turbulent flows. As a matter of fact, a great deal of numerical work is at present being performed to elucidate the concentration of vorticity on very fine filaments, either in the case of homogeneous turbulence (e.g. Jimenez *et al.* 1993) or in the case of shear flows (e.g. among several other authors, Comte, Lesieur & Lamballais 1992; Silvestrini, Comte & Lesieur 1994). In some cases, for instance in the two last papers, the pressure distribution is calculated and the results are given as pressure probability density functions at different instants of the temporal mixing layer evolution. The conditions of incipient cavitation into the near-wake vortices allow us to estimate one point of such curves. That is done below, under the assumption that the dead water region (A, see figure 5) is limited by two simple plane mixing layers in which the flow is mainly two-dimensional.

Let us consider for example the case of cavitation inception with a Reynolds number equal to 2.2×10^5 for which the velocity V_c is about 6.3 m s^{-1} and V_s is 9.9 m s^{-1}. Then, the boundary layer thickness is $\delta_s = 0.56$ mm, and the initial wavelength is $\lambda_s = 4.6$ mm. The difference between the incipient cavitation number and the base pressure coefficient C_{p_s} is considered as the crest value of the fluctuating underpressure which would be calculated by numerical methods. It is estimated from figure 16 as about 5.

With the notation used in numerical studies, the pressure coefficient is related to the term ρU^2, where U is the half-difference between both fluid layer velocities (here $U = V_s/2 = 4.95\ \mathrm{m\ s^{-1}}$), while our pressure coefficient is scaled by $\rho V_2^2/2$. Taking into account those differences, we find a new value very close to 4 for the maximum underpressure coefficient.

Such a value could be validly compared to the results of calculations if significant Reynolds numbers were approximately the same in both cases. That is not possible at the present time and we can only put the experimental results beside the numerical ones, noting however the Reynolds number values in each case. In their study, Silvestrini *et al.* (1994) find values of the minimum pressure coefficient in the range -1.6 to -1.1, according to the subgrid turbulence model used, for a probability equal to 10^{-5}. The theoretical Reynolds number $U\delta_i/\nu$, in which δ_i is used for the scaling of the initial velocity gradient, is equal to 100; in our case, taking $\delta_i = \delta_{1s}$, the corresponding Reynolds number is 960. If we consider another experimental point, situated on the left of figure 16 and corresponding to $Re = 1.4 \times 10^5$, we have $U\delta_{1s}/\nu = 770$; the maximum underpressure coefficient is 3.2.

To estimate the probability of minimum pressure occurrence, we need both the volume of liquid which sustains that pressure and the volume of reference. In view of the practically two-dimensional present situation, surfaces areas must be considered instead. In a way similar to the one used in temporal numerical simulations, we can take a reference rectangle with a streamwise side equal to $2\lambda_s$ and a transverse side scaled by λ_s or δ_s. Returning to the first experimental point above, we choose $2\lambda_s$ – which here is equivalent to $16\delta_s$ – thus obtaining a reference area of 85 mm^2. The minimum pressure region area can be estimated from the arguments displayed in §2, which give diameters of the order 2 μm – or maybe a little more if one considers that the liquid core to be turned into vapour is less than the region in which pressure is very close to its minimum value. Then, the probability we look for is 4×10^{-8} at least and possibly can be raised by a coefficient between 10 and 100. Thus, it is possible that differences between experimental and numerical results on minimum pressure coefficients are due to the size of the mesh used in simulations.

Further information is available from our experiments: over the whole region A on which they are visible, the near-wake vortices do not display any three-dimensional instability and indeed no streamwise vortices appear. In temporal numerical simulations, the time increment is $\Delta t = \delta_i/U$, and intense enough streamwise vortices are found from the time $14\Delta t$. For comparison, the length L of region A can be converted into a time available for the vortex evolution by considering the ratio L/V_s. Taking $\delta_i = \delta_s$, we obtain a total time equal to $\Delta t L/(2\delta_s)$, i.e. about $23\Delta t$ with $L = 25$ mm. Thus, it would appear that the three-dimensional instability is less strong than the one anticipated in the numerical simulation.

8. Conclusions

In conclusion, visualization techniques, although limited in their resolution capacity, allow us to obtain evidence for three kinds of rotational structures in the cavitating turbulent wake of a wedge-shaped obstacle: the primary spanwise vortices, the secondary streamwise vortices and the near-wake vortices. The latter are also called *shear layer vortices* (Kourta *et al.* 1987, among others) because of their separation in coherent structures when exposed to the strong instability of the shear layers which limit the dead fluid downstream of the blunt obstacle.

Cavitation does not behave as a passive agent with regard to the basic flow but it

tends to modify its global features: for instance, the Strouhal number strongly depends on the development of cavitation, as does the distance between the two rows of primary, Bénard–Kármán, vortices. Cavitation also adds some complication to local mechanisms: on the one hand, it breaks the connection between the elongation rate of the vortex filaments and their rotation rate and, on the other hand, it affects the translational velocity of the cavitating rotational structures by an effect of added mass. However, it must be noted that in conditions of incipient cavitation, information useful for the basic turbulent flow can be obtained, just as discussed in §7.

A two-dimensional model based on the near-wake vortices is proposed. It leads to a forecast of the inception cavitation parameter σ_i corroborated well by the experimental results. The success of the method is closely connected to the counting of the cavitating near-wake vortices, which is made possible by rapid cinematography and which shows that their initial wavelength approximately corresponds to the most unstable mode of the free shear layer. Thus, consideration of the coherent rotational structures is likely the best way to explain, in an almost deterministic way, the large difference between the absolute value of the mean pressure coefficient at the obstacle base and the incipient cavitation number.

This work was partially supported by the French Army Department under contract number DRET 87/096. We wish to thank M. Marchadier and G. Brault for their technical assistance during the experimental tests. We had fruitful discussions with people of our laboratory familiar with basic problems of turbulent flows: among them, Y. Gagne, and the staff of numerical simulation of turbulence, namely M. Lesieur, O. Métais, P. Comte and J. H. Silvestrini. Finally, we wish to express our gratitude to Miss E. G. Filali who kindly allowed us to use the result she established concerning the streamwise vortices in the far wake.

REFERENCES

ARNDT, R. E. A. 1976 Semi-empirical analysis of cavitation in the wake of a sharp-edged disk. *Trans. ASME* I: *J. Fluids Engng* **98**, 560–562.

ARNDT, R. E. A., ARAKERI, V. H. & HIGUCHI, H. 1991 Some observations of tip-vortex cavitation. *J. Fluid Mech.* **229**, 269–289.

BATCHELOR, G. K. 1967 *An Introduction to Fluid Dynamics*. Cambridge University Press.

BELAHADJI, B. 1993 Cavitation dans le sillage turbulent d'un obstacle. PhD thesis, Université Joseph Fourier, Grenoble.

BELAHADJI, B., FRANC, J. P. & MICHEL, J. M. 1993 Cavitation naissante dans un sillage turbulent et tourbillons de couche limite. *Quatrième J. Hydrodyn. Nantes, Proc.*, pp. 117–120. Inst. Français du Pétrole.

BERGER, E. & WILLE, R. 1972 Periodic flow phenomena. *Ann. Rev. Fluid Mech.* **4**, 313–340.

BERNAL, L. P. & ROSHKO, A. 1986 Streamwise vortex structure in plane mixing layers. *J. Fluid Mech.* **170**, 499–525.

BRIANÇON-MARJOLLET, L., FRANC, J. P. & MICHEL, J. M. 1990 Transient bubbles interacting with an attached cavity and the boundary layer. *J. Fluid Mech.* **218**, 355–376.

BRIANÇON-MARJOLLET, L. & MICHEL, J. M. 1990 The hydrodynamic tunnel of I.M.G.: former and recent equipment. *Trans. ASME* I: *J. Fluids Engng* **112**, 338–342.

COMTE, P., LESIEUR, M. & LAMBALLAIS, E. 1992 Large- and small-scale stirring of vorticity and a passive scalar in a 3-D temporal mixing layer. *Phys. Fluids* A **4**, 2761–2778.

CORCOS, G. M. & LIN, S. J. 1984 The mixing layer: deterministic models of a turbulent flow. Part 2. The origin of the three-dimensional motion. *J. Fluid Mech.* **139**, 67–95.

DOUADY, S., COUDER, Y. & BRACHET, M. E. 1991 Direct observation of the intermittency of intense vorticity filaments in turbulence. *Phys. Rev. Lett.* **67**, 983–986.

DRAZIN, P. G. & REID, W. H. 1981 *Hydrodynamic Stability*. Cambridge University Press.

FILALI, E. G. 1993 Analyse des tourbillons cavitants formés dans le sillage d'un coin. *Institut National Polytechnique de Grenoble, DEA Rep.*

FRANC, J. P. 1982 Étude de cavitation, tome 2: Sillage cavitant d'obstacles épais. PhD thesis, Institut National Polytechnique de Grenoble, pp. 66–121.

FRANC, J. P., MICHEL, J. M. & LESIEUR, M. 1982 Structures rotationnelles bi et tri-dimensionnelles dans un sillage cavitant. *C.R. Acad. Sci. Paris* **295**, 773–777.

FRUMAN, D. H., DUGUÉ, C., PAUCHET, A., CERRUTTI, P. & BRIANÇON-MARJOLLET, L. 1992 Tip vortex roll-up and cavitation. *Proc. ONR Cong. Seoul, Korea.* ONR.

GENOUX, P. & CHAHINE, G. L. 1983 Équilibre statique et dynamique d'un tore de vapeur tourbillonnaire. *J. Méc. Théor. Appl.* **2**, 829–857.

JIMENEZ, J., WRAY, A. A., SAFFMAN, P. G. & ROGALLO, R. S. 1993 The structure of intense vorticity in isotropic turbulence. *J. Fluid Mech.* **255**, 65–90.

KATZ, J. & O'HERN, T. J. 1986 Cavitation in large scale shear flows. *Trans. ASME* I: *J. Fluids Engng* **108**, 373–376.

KERMEEN, R. W. & PARKIN, B. R. 1957 Incipient cavitation and wake flow behind sharp-edged disks. *Calif. Inst. of Tech. Engng Div. Rep.* 85–4.

KNAPP, R. T., DAILY, J. W. & HAMMITT, F. G. 1970 *Cavitation*. McGraw Hill.

KOURTA, A., BOISSON, H. C., CHASSAING, P. & HA MINH, H. 1987 Nonlinear interaction and the transition to turbulence in the wake of a circular cylinder. *J. Fluid Mech.* **181**, 141–161.

LASHERAS, J. C., CHO, J. S. & MAXWORTHY, T. 1986 On the origin and evolution of streamwise vortical structures in a plane, free shear layer. *J. Fluid Mech.* **172**, 231–258.

LASHERAS, J. C. & CHOI, H. 1988 Three-dimensional instability of a plane free shear layer: an experimental study of the formation and evolution of streamwise vortices. *J. Fluid Mech.* **189**, 53–86.

LESIEUR, M. 1993 *Turbulence in Fluids*, 2nd edn. Kluwer.

LIEPMAN, D. & GHARIB, M. 1992 The role of streamwise vorticity in the near-field entrainment of round jets. *J. Fluid Mech.* **245**, 643–668.

LIGNEUL, P. 1989 Theoretical tip vortex cavitation inception threshold. *Eur. J. Mech.* B/*Fluids* **8**, 495–521.

LIN, S. J. & CORCOS, G. M. 1984 The mixing layer: deterministic models of a turbulent flow. Part 3. The effect of a plane strain on the dynamics of streamwise vortices. *J. Fluid Mech.* **141**, 139–178.

MEIBURG, E. & LASHERAS, J. C. 1988 Experimental and numerical investigation of the three-dimensional transition in plane wakes. *J. Fluid Mech.* **190**, 1–37.

MÉTAIS, O. & LESIEUR, M. 1992 Spectral large-eddy simulation of isotropic and stably stratified turbulence. *J. Fluid Mech.* **239**, 157–194.

MILNE-THOMSON, L. M. 1968 *Theoretical Hydrodynamic*, 5th edn, pp. 377–380. Macmillan.

PAUCHET, J., RETAILLEAU, A. & WOILLEZ, J. 1992 The prediction of cavitation inception in turbulent water jets. *Cavitation and Multiphase Flow Forum*, ASME FED, vol. **135**, pp. 149–158.

RAMAMURTHY, A. S. & BALACHANDAR, R. 1990 The near wake characteristics of cavitating bluff sources. *Trans. ASME* I: *J. Fluids Engng* **112**, 492–495.

ROSHKO, A. 1954 On the development of turbulent wakes from vortex streets. *NACA Rep.* 1191.

SCHLICHTING, H. 1987 *Boundary layer Theory*. McGraw-Hill.

SILVESTRINI, J. H., COMTE, P. & LESIEUR, M. 1994 Large-eddy simulation of periodic incompressible mixing layers. *Preprint LEGI-IMG* (to be submitted to *Eur. J. Mech.*).

SOYAMA, H., KATO, H. & OBA, R. 1992 Cavitation observations of severely erosive vortex arising in a centrifugal pump. *Proc. Intl Conf. on Cavitation, I. Mech. E., Cambridge*, pp. 103–110.

YOUNG, A. J. & HOLL, W. J. 1966 Effects of cavitation on periodic wakes behind symmetric wedges. *Trans. ASME* D: *J. Basic Engng*, 163–176.